International Journal of Rock Mechanics & Mining Sciences xxx (xxxx) xxx

Contents lists available at ScienceDirect

International Journal of Rock Mechanics and Mining Sciences

journal homepage: www.elsevier.com/locate/ijrmms

Open-pit slope design using a DtN-FEM: Parameter space exploration

Mario Durán [a], Eduardo Godoy [b,*], Esteban Román Catafau [c,d], Patricio A. Toledo [e]

[a] Departamento de Ingeniería Matemática, Universidad de Concepción, Casilla 160-C, Concepción, Chile
[b] INGMAT R&D Centre, José Miguel de la Barra 412, 4to piso, Santiago, Chile
[c] Department of Mechanical Engineering, National Cheng Kung University, No 1 University Road, Tainan, 70101, Taiwan
[d] Universidad Adolfo Ibáñez, Av. Diagonal Las Torres 2640, Peñalolén, Santiago, Chile
[e] Programa de Riesgo Sísmico, Universidad de Chile, Beaucheff 850, Santiago, Chile

ARTICLE INFO

Keywords:
Dirichlet-to-Neumann map
Finite elements
Open-pit
Slope design

ABSTRACT

Given the sustained mineral-deposits ore-grade decrease, it becomes necessary to reach greater depths when extracting ore by open-pit mining. Steeper slope angles are thus likely to be required, leading to geomechanical instabilities. In order to determine excavation stability, mathematical modelling and numerical simulation are often used to compute the rock-mass stress-state, to which some stability criterion needs to be added. A problem with this approach is that the volume surrounding the excavation has no clear borders and in practice it might be regarded as an unbounded region. Then, it is necessary to use advanced methods capable of dealing efficiently with this difficulty. In this work, a DtN-FEM procedure is applied to calculate displacements and stresses in open-pit slopes under geostatic stress conditions. This procedure was previously devised by the authors to numerically treat this kind of problems where the surrounding domain is semi-infinite. Its efficiency makes possible to simulate, in a short amount of time, multiple open-pit slope configurations. Therefore, the method potentiality for open-pit slope design is investigated. A regular open-pit slope geometry is assumed, parameterised by the overall-slope and bench-face angles. Multiple geometrically admissible slopes are explored and their stability is assessed by using the computed stress-field and the Mohr–Coulomb failure criterion. Regions of stability and instability are thus explored in the parametric space, opening the way for a new and flexible designing tool for open-pit slopes and related problems.

1. Introduction

Due to the sustained ore grade decrease in mineral deposits, mine depth is increasing, leading to steeper slopes. A likely consequence of this is geomechanical instability, with adverse effects in terms of lower mineral resources and reserves, loss of equipment, time and risks to workers. A possible control measure for the effects of instability is a precise knowledge of the rock-mass stress-state surrounding the mine. The use of computer simulation by means of numerical methods can significantly help to achieve this purpose.

In general, when applying numerical methods to calculate stresses, a computational domain needs to be established, which corresponds to the spatial region where the computations will be done. However, in the case of a mine (or any excavation) it is not clear a priori how large that computational domain should be. In practice, all the surroundings can be regarded as unbounded, but computers cannot store infinite domains. A popular and heuristic approach to overcome this difficulty is to employ a huge domain, typically a rectangular box, with its external boundaries far away enough from the mine so that they have minimal effect on the results to be computed. The discretisation of such a domain requires a large amount of points, making the numerical method performance inefficient and even inaccurate, mainly due to abuses in boundary conditions. A single simulation of a detailed 3D mine can take up days to yield meaningful results.

A comprehensive survey of numerical approaches to solve problems formulated in unbounded domains is provided in Ref. 1. This kind of methods are classified into four main categories: boundary integral equation methods, absorbing layer methods, infinite element methods, and artificial boundary condition (ABC) methods. All these kinds of methods are well-suited to treat infinite exterior domains, that is, the whole space minus some bounded region, which are relatively simple as they are unbounded in all directions and its boundary is finite. However, in geomechanical applications such as the stress-state in an excavation, the domain is normally assumed to be a half-space minus a bounded region, that is, a semi-infinite domain. This type of domain has

* Corresponding author.
E-mail addresses: maduran@ing-mat.udec.cl (M. Durán), eduardo.godoy@ingmat.com (E. Godoy), esteban.roman@nordlinglab.org (E. Román Catafau), ptoledo@dgf.uchile.cl (P.A. Toledo).

https://doi.org/10.1016/j.ijrmms.2021.104950
Received 15 April 2021; Received in revised form 24 September 2021; Accepted 26 October 2021

some additional difficulties since it is bounded only in some directions and it has an infinite boundary, where some boundary condition is prescribed. The numerical method to be employed should be able to deal with these difficulties, so it may require some adaptations.

Boundary integral equations and the boundary element method (BEM) have been successfully applied to infinite exterior domains and there is a vast literature on the subject. These kind of methods have the advantage of reducing the dimensionality of the problem by one. However, to be applied to semi-infinite domains in a computationally efficient way (avoiding discretisation of an infinite boundary), a half-space fundamental solution is required, which may not be explicitly available in some cases. BEM solutions for elasticity in a half-plane can be found in Refs. 2, 3, where a half-plane fundamental solution is used. In a more recent work Ref. 4, a BEM formulation for the elastic half-space in the axisymmetric case is presented, which uses an axisymmetric fundamental solution for the elastic half-space, given in terms of integrals of the Lipschitz–Hankel type.

Infinite element methods have also been widely used to treat infinite and semi-infinite domains. The advantage of these methods is their simplicity, as the concept of infinite element is the same as that of finite element, except for the infinity of the element domain. However, some issues need to be resolved, such as the right choice of shape functions in order to reflect the asymptotic behaviour of the solution at infinity, as well as the numerical calculation of some integrals over infinite domains. Improved infinite elements based on mapping is proposed in Ref. 5, which are tested on the axisymmetric problem of a point load on an elastic half-space. In a recent work Ref. 6, introduces an approach that combines some features of infinite elements with the numerical manifold method, where the usual shape functions are substituted by infinite patches with the weight functions satisfying the partition of unity. This technique is tested in half-space elasticity problems.

A powerful numerical technique, belonging to the ABC category, is the DtN-FEM (Dirichlet-to-Neumann finite element method), where finite elements are used in combination with the so-called DtN map, defined over an artificial boundary.[7–9] The main advantage of this approach is that the DtN map provides *exact boundary conditions*, ensuring continuity of the solution and its derivatives across the artificial boundary, which results in a method with high accuracy. In general, it is possible to apply this type of procedure on the condition that an explicit, analytical closed-form expression for the DtN map exists. Such is the case for most infinite exterior problems.[10–13] However, applying the DtN-FEM to a semi-infinite domain could be tricky, mainly due to the lack of closed-form expressions for the DtN map in most cases of interest, therefore some approximation of it becomes necessary.[14–16]

In a relatively recent work,[17] the authors presented a DtN-FEM approach for axisymmetric problems in an elastic half-space, based on a suitable approximation of the associated DtN map obtained through a semi-analytical procedure, also developed by the authors in a previous paper.[18] The coupling between the DtN map, expressed in series form, and the FEM scheme is done directly on the discretised variational formulation of the boundary-value problem, specifically on the boundary integral terms on a semi-spherical artificial boundary. In order to validate the method, a model problem was used, consisting in a simplified case with exact analytical solution. The relative error between numerical and exact solution was studied in terms of artificial boundary location, number of terms in the DtN map series and mesh size. The method exhibited an excellent performance in terms of flexibility, speed, precision and robustness. The achieved accuracy was satisfactory even for close artificial boundaries, small number of terms in the series and coarse meshes.

This paper aims at exploiting the advantages of this DtN-FEM by solving a problem in open-pit slope design which requires to solve several cases. A homogeneous, isotropic and fully fractured rock-mass is mined with an open-pit having regular axisymmetric slope, and fixed number of benches and overall slope height as well, whereas overall-slope angle and bench-face angle are variable parameters. Regions of geomechanical stability/instability are thus determined in the parametric space by exploring Mohr–Coulomb failure criterion given the geometry-induced stress-field.

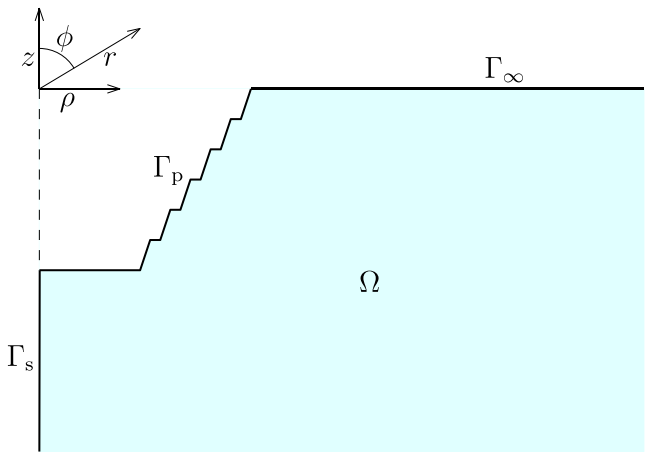

Fig. 1. Locally perturbed semi-infinite domain (axisymmetric cross-section).

2. Overview of DtN-FEM

2.1. Preliminaries

In what follows, an overview of the DtN-FEM approach is given. Full details are found in Ref. 17. Let us consider the lower half-space, described in cylindrical coordinates (ρ, θ, z) as the region in $\mathbb{R}^3$ where $\rho \geq 0$ and $z < 0$, or alternatively in spherical coordinates (r, θ, ϕ) as the region in $\mathbb{R}^3$ where $r > 0$ and $\pi/2 < \phi < \pi$. Notice that this semi-infinite region is axisymmetric with respect to the z-axis, and in particular it does not depend on the azimuthal angle θ. We assume that an axisymmetric open-pit is introduced at the half-space centre, which is regarded as a local geometrical perturbation of its surface. The resulting locally perturbed semi-infinite domain is completely described by its axisymmetric cross-section, which corresponds to a 2D domain which we denote by Ω. (see Fig. 1). Its boundary $\partial\Omega$ consists of a flat part Γ_∞ that extends to infinity, a vertical part Γ_s that coincides with the z-axis, and a perturbed bounded part Γ_p that corresponds to the open-pit boundary. The domain Ω will be described in cylindrical coordinates (ρ, z) or spherical coordinates (r, ϕ) as appropriate. The associated unit vectors are denoted by $(\hat{\boldsymbol{\rho}}, \hat{\boldsymbol{z}})$ and $(\hat{\boldsymbol{r}}, \hat{\boldsymbol{\phi}})$, respectively.

2.2. Mathematical model

We assume that Ω is occupied by a homogeneous, isotropic, linear elastic rock-mass, with micro-fractures in all directions. Let us denote by $\boldsymbol{u} = (u_\rho, u_z)^T$ the displacement field and by $\boldsymbol{\varepsilon} = (\varepsilon_\rho, \varepsilon_z, \varepsilon_\theta, \varepsilon_{\rho z})^T$ the strain tensor. In the axisymmetric case, $\boldsymbol{\varepsilon}$ has four components (cf. Ref. 19), which are defined as:

$$\varepsilon_\rho = \frac{\partial u_\rho}{\partial \rho}, \quad \varepsilon_z = \frac{\partial u_z}{\partial z}, \quad \varepsilon_\theta = \frac{u_\rho}{\rho}, \quad \varepsilon_{\rho z} = \frac{1}{2}\left(\frac{\partial u_\rho}{\partial z} + \frac{\partial u_z}{\partial \rho}\right). \tag{1}$$

The stress tensor $\boldsymbol{\sigma} = (\sigma_\rho, \sigma_z, \sigma_\theta, \sigma_{\rho z})^T$ is given in terms of $\boldsymbol{\varepsilon}$ by the isotropic Hooke law. Its components are:

$$\sigma_\rho = \lambda(\varepsilon_\rho + \varepsilon_z + \varepsilon_\theta) + 2\mu\varepsilon_\rho, \tag{2a}$$

$$\sigma_z = \lambda(\varepsilon_\rho + \varepsilon_z + \varepsilon_\theta) + 2\mu\varepsilon_z, \tag{2b}$$

$$\sigma_\theta = \lambda(\varepsilon_\rho + \varepsilon_z + \varepsilon_\theta) + 2\mu\varepsilon_\theta, \tag{2c}$$

$$\sigma_{\rho z} = 2\mu\varepsilon_{\rho z}, \tag{2d}$$

where λ, μ are Lamé's constants of the medium, which is also characterised by Young modulus E and Poisson ratio ν. Both pairs of elastic constants are linked by:

$$\lambda = \frac{\nu E}{(1+\nu)(1-2\nu)}, \qquad \mu = \frac{E}{2(1+\nu)}. \tag{3}$$

In addition, we assume that the rock-mass is subjected to an initial stress $\boldsymbol{\sigma}^{ini}$. The total stress, given by $\boldsymbol{\sigma}^{tot} = \boldsymbol{\sigma} + \boldsymbol{\sigma}^{ini}$, then satisfies the elastic equilibrium equation in Ω, that is:

$$\nabla \cdot \boldsymbol{\sigma}^{tot} = \varrho g \hat{\boldsymbol{z}}, \tag{4}$$

where ϱ denotes the solid-medium mass-density and g is the gravity acceleration. The right-hand side of (4) accounts for the solid weight. Moreover, the physical boundary of Ω, composed by Γ_{p} and Γ_∞ is supposed traction-free, that is:

$$\boldsymbol{\sigma}^{tot}\hat{\boldsymbol{n}} = \boldsymbol{0}, \tag{5}$$

where $\hat{\boldsymbol{n}}$ is the outward unit vector normal to the boundary, which coincides with $\hat{\boldsymbol{z}}$ on Γ_∞. Regarding the initial stress, we assume a stress-state including geostatic and tectonic loads. Vertical stress σ_z^{ini} and horizontal stress σ_ρ^{ini} are thus given by:

$$\sigma_z^{ini} = \varrho g z, \qquad \sigma_\rho^{ini} = k_0 \sigma_z^{ini}, \tag{6}$$

where k_0 is the coefficient of lateral Earth pressure. The particular case $k_0 = \lambda/(\lambda+2\mu)$ represents pure geostatic stress. Any other positive value of k_0 implies some tectonic stress. The remaining components σ_θ^{ini} and $\sigma_{\rho z}^{ini}$ are zero. Expressing (4) and (5) in terms of the stress $\boldsymbol{\sigma}$, and using that $\nabla \cdot \boldsymbol{\sigma}^{ini} = \varrho g \hat{\boldsymbol{z}}$ and $\boldsymbol{\sigma}^{ini} = \boldsymbol{0}$ for $z = 0$ (both identities are easily verified), we arrive at the following boundary-value problem in Ω: Find $\boldsymbol{u} : \Omega \to \mathbb{R}^2$ such that:

$$\nabla \cdot \boldsymbol{\sigma} = \boldsymbol{0} \qquad \text{in } \Omega, \tag{7a}$$
$$\boldsymbol{\sigma}\hat{\boldsymbol{z}} = \boldsymbol{0} \qquad \text{on } \Gamma_\infty, \tag{7b}$$
$$\boldsymbol{\sigma}\hat{\boldsymbol{n}} = \boldsymbol{f} \qquad \text{on } \Gamma_{\mathrm{p}}, \tag{7c}$$
$$\sigma_{\rho z} = u_\rho = 0 \qquad \text{on } \Gamma_{\mathrm{s}}, \tag{7d}$$
$$|\boldsymbol{u}| = O\big(r^{-1}\big) \qquad \text{as } r \to \infty, \tag{7e}$$

where $\boldsymbol{f} = -\boldsymbol{\sigma}^{ini}\hat{\boldsymbol{n}}$. Expressing the equations in terms of $\boldsymbol{\sigma}$ instead of $\boldsymbol{\sigma}^{tot}$ has the advantage that the elastic equilibrium equation (7a) has zero right-hand side. In addition, the traction-free boundary condition on Γ_∞ (7b) keeps a zero right-hand side, whereas a nonzero forcing term arises in the boundary condition on Γ_{p} (7c), due to the change of variable. The boundary-value problem is completed with a condition on Γ_{s} (7d), which in order to preserve the axisymmetry must be constrained against horizontal displacement, shear-free traction, and a decaying condition at infinity for $\boldsymbol{u}$ (7e).

2.3. Equivalent bounded problem

In order to apply our DtN-FEM approach to solve (7), the unbounded domain Ω is truncated by a semi-spherical artificial boundary. Two new domains are obtained: a bounded interior computational domain Ω^i and an unbounded exterior domain Ω^e, as indicated in Fig. 2. The truncation radius is denoted by R. Notice that the artificial boundary, denoted by Γ_R, simply corresponds to a quarter of circumference. Boundaries Γ_∞ and Γ_{s} are split into bounded parts Γ_∞^i and Γ_{s}^i, and unbounded parts Γ_∞^e and Γ_{s}^e, respectively. Problem (7) is restated in the computational domain, leading to the following boundary-value problem: Find $\boldsymbol{u} : \Omega^i \to \mathbb{R}^2$ such that:

$$\nabla \cdot \boldsymbol{\sigma} = \boldsymbol{0} \qquad \text{in } \Omega^i, \tag{8a}$$
$$\boldsymbol{\sigma}\hat{\boldsymbol{z}} = \boldsymbol{0} \qquad \text{on } \Gamma_\infty^i, \tag{8b}$$
$$\boldsymbol{\sigma}\hat{\boldsymbol{n}} = \boldsymbol{f} \qquad \text{on } \Gamma_{\mathrm{p}}, \tag{8c}$$
$$\sigma_{\rho z} = u_\rho = 0 \qquad \text{on } \Gamma_s^i, \tag{8d}$$
$$\boldsymbol{\sigma}\hat{\boldsymbol{r}} = -\mathcal{M}\boldsymbol{u} \qquad \text{on } \Gamma_R, \tag{8e}$$

where $\mathcal{M}$ denotes de DtN map of the elastic half-space, which for the moment is assumed to be known. To state a variational (or weak) formulation of (8), we consider the Sobolev space $\mathcal{V}$ consisting of physically admissible vector functions $\boldsymbol{v} : \Omega \to \mathbb{R}^2$, with both components v_ρ, v_z in $H^1(\Omega)$ and v_ρ with zero trace on Γ_s. The variational formulation of (8) reads: Find $\boldsymbol{u} \in \mathcal{V}$ such that:

$$a(\boldsymbol{u},\boldsymbol{v}) + \int_{\Gamma_R} \mathcal{M}\boldsymbol{u}\cdot\boldsymbol{v}\,\mathrm{d}\Gamma_R = \int_{\Gamma_{\mathrm{p}}} \boldsymbol{f}\cdot\boldsymbol{v}\,\mathrm{d}\Gamma_{\mathrm{p}} \qquad \forall\,\boldsymbol{v}\in\mathcal{V}, \tag{9}$$

where a corresponds to the bilinear form of axisymmetric linear elasticity, which is standard. The integral term on the left-hand side of (9) accounts for the contribution of DtN map, being the non-standard part of the weak formulation.

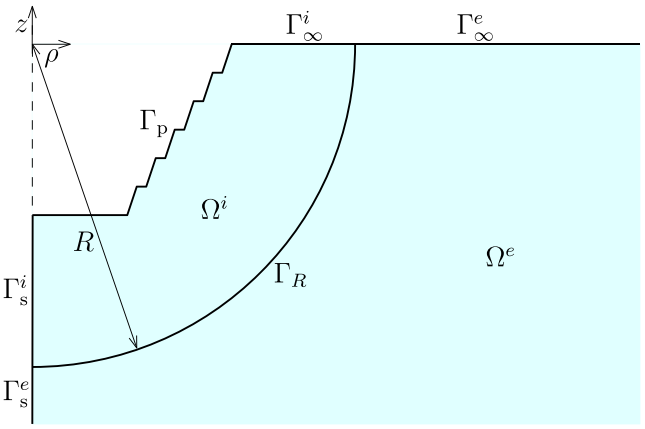

Fig. 2. Truncated domain.

2.4. FEM discretisation

Let us consider a standard FEM discretisation of (9) using $P1$ triangular elements. Given a triangular mesh of Ω, its size is denoted by h. The components of the discrete vector solution $\boldsymbol{u}_h$ are then sought in a finite-dimensional space $\mathcal{V}_h \subset \mathcal{V}$ consisting of continuous, piecewise linear functions, whose dimension is denoted by N_h. The usual basis for $\mathcal{V}_h$ is composed by nodal shape functions $\{\psi_i\}_{i=1}^{N_h}$ such that $\psi_i = 1$ at node i and $\psi_i = 0$ at all node $j \neq i$. The solution is thus expressed as:

$$\boldsymbol{u}_h = \sum_{i=1}^{N_h} (d_{\rho i}\hat{\boldsymbol{\rho}} + d_{zi}\hat{\boldsymbol{z}})\psi_i, \tag{10}$$

where $d_{\rho i}$ and d_{zi} are the unknown nodal values associated with components in ρ and z of the discrete solution $\boldsymbol{u}_h$, respectively. Substitution of (10) in (9) leads to its matrix form, expressed as:

$$\boldsymbol{K}\boldsymbol{d} = \boldsymbol{F}, \tag{11}$$

where the right-hand side $\boldsymbol{F}$ comes from the right-hand side discretisation of (9), and $\boldsymbol{d}$ is a vector containing the unknown coefficients $d_{\rho i}, d_{zi}$. The matrix of the system is written as:

$$\boldsymbol{K} = \boldsymbol{K}^a + \boldsymbol{K}^b, \tag{12}$$

where $\boldsymbol{K}^a$ comes from the bilinear form discretisation a and $\boldsymbol{K}^b$ is related to the integral term on Γ_R in (9). Matrix $\boldsymbol{K}^a$ and vector $\boldsymbol{F}$ are computed by Gauss numerical integration, whereas the evaluation of matrix $\boldsymbol{K}^b$ requires a special procedure. This matrix has size $2N_h$, and is defined by blocks as:

$$\boldsymbol{K}^b = \begin{bmatrix} \boldsymbol{K}^b_{\rho\rho} & \boldsymbol{K}^b_{\rho z} \\ \boldsymbol{K}^b_{z\rho} & \boldsymbol{K}^b_{zz} \end{bmatrix}. \tag{13}$$

These four blocks are defined through their ij-components as:

$$[\boldsymbol{K}^b_{\alpha\beta}]_{ij} = \int_{\Gamma_R} \psi_i \hat{\boldsymbol{\alpha}}\cdot\mathcal{M}\psi_j\hat{\boldsymbol{\beta}}\,\mathrm{d}\Gamma_R, \qquad \alpha,\beta = \rho, z, \tag{14}$$

which are nonzero only if both nodes i and j lie on the artificial boundary Γ_R. Therefore, and recalling that there is no explicit closed-form expression for the DtN map $\mathcal{M}$, highly accurate numerical approximations of terms $\mathcal{M}\psi_j\hat{\boldsymbol{\rho}}$ and $\mathcal{M}\psi_j\hat{\boldsymbol{z}}$, for every node j lying on Γ_R, are required in order to fully solve the boundary-value problem (8).

2.5. Semi-analytical DtN map approximation

To approximate the integral terms (14), we start by giving the mathematical DtN map definition. Given any displacement $\boldsymbol{v} \in \mathcal{V}$, with trace $\boldsymbol{v}|_{\Gamma_R} \in [H^{1/2}(\Gamma_R)]^2$, we define $\mathcal{M}\boldsymbol{v} = -\boldsymbol{\sigma}\hat{\boldsymbol{r}}|_{\Gamma_R} \in [H^{-1/2}(\Gamma_R)]^2$, where $\boldsymbol{\sigma}$ is the stress tensor whose components are computed through (1) and (2) from the displacement $\boldsymbol{u}$, the solution of the following boundary-value problem stated in the exterior domain: Find $\boldsymbol{u} : \Omega^e \to \mathbb{R}^2$ such that:

$$\nabla \cdot \boldsymbol{\sigma} = \boldsymbol{0} \qquad \text{in } \Omega^e, \tag{15a}$$

$$\boldsymbol{\sigma}\hat{\boldsymbol{z}} = \boldsymbol{0} \qquad \text{on } \Gamma^e_\infty, \tag{15b}$$

$$\boldsymbol{u} = \boldsymbol{v} \qquad \text{on } \Gamma_R, \tag{15c}$$

$$\sigma_{\rho z} = u_\rho = 0 \qquad \text{on } \Gamma^e_s, \tag{15d}$$

$$|\boldsymbol{u}| = O\left(r^{-1}\right) \qquad \text{as } r \to \infty, \tag{15e}$$

which needs to be solved for $\boldsymbol{v} = \psi_j\hat{\boldsymbol{\rho}}$ and $\boldsymbol{v} = \psi_j\hat{\boldsymbol{z}}$. The technique to do so, fully described in Refs. 17, 18, is based upon an enhanced version of the solution originally proposed by Eubanks.[20] By using Papkovich–Neuber potentials and separation of variables in spherical coordinates (r, ϕ), it is possible to find a general analytical solution to (15) in series form, which is expressed as:

$$\boldsymbol{u}(r,\phi) = \sum_{n=0}^{\infty} A_n \left(\frac{R}{r}\right)^{2n+2} \boldsymbol{w}_n^{(A)}(\phi) + \sum_{n=-1}^{\infty} B_n \left(\frac{R}{r}\right)^{2n+3} \boldsymbol{w}_n^{(B)}(\phi), \tag{16}$$

where $\boldsymbol{w}_n^{(A)}(\cdot)$ and $\boldsymbol{w}_n^{(B)}(\cdot)$ are known vector functions and coefficients A_n and B_n are arbitrary. The associated stress tensor $\boldsymbol{\sigma}$ is written as:

$$\boldsymbol{\sigma}(r,\phi) = \frac{1}{R}\left[\sum_{n=0}^{\infty} A_n \left(\frac{R}{r}\right)^{2n+3} \boldsymbol{\tau}_n^{(A)}(\phi) + \sum_{n=-1}^{\infty} B_n \left(\frac{R}{r}\right)^{2n+4} \boldsymbol{\tau}_n^{(B)}(\phi)\right], \tag{17}$$

where $\boldsymbol{\tau}_n^{(A)}(\cdot)$ and $\boldsymbol{\tau}_n^{(B)}(\cdot)$ are known tensor functions. The explicit expressions for these vector and tensor functions are provided in Appendix. This solution, in its series form (16)–(17), satisfies (15a), (15b), (15d) and (15e). In order for it to satisfy (15c), coefficients A_n and B_n needs to be determined as a function of the Dirichlet datum $\boldsymbol{v}$. This is not possible in a fully analytical way, so it is done numerically. To that purpose, we define the following energy functional $\mathcal{J}$:

$$\mathcal{J}(\boldsymbol{u}) = -\frac{1}{2R}\int_{\Gamma_R} \boldsymbol{\sigma}\hat{\boldsymbol{r}} \cdot \boldsymbol{u}\, \mathrm{d}\Gamma_R + \frac{1}{R}\int_{\Gamma_R} \boldsymbol{\sigma}\hat{\boldsymbol{r}} \cdot \boldsymbol{v}\, \mathrm{d}\Gamma_R, \tag{18}$$

where $\boldsymbol{u}$ and $\boldsymbol{\sigma}$ are given in the particular series forms (16) and (17), in such a way that $\mathcal{J}$ is actually a function of the undetermined coefficients A_n and B_n. Thus, the first term in (18) is quadratic in A_n, B_n and the second term is linear in A_n, B_n. The quadratic term is also positive definite (notice that the unit normal vector pointing outwards Ω^e corresponds to $-\hat{\boldsymbol{r}}$) and represents the surface elastic potential energy on Γ_R. The linear term is directly related to the Dirichlet datum $\boldsymbol{v}$ prescribed on Γ_R. With $\mathcal{J}$ defined in this way, it reaches its minimum when (15c) holds (See Refs. 17, 18 for more details). Substituting (16)–(17) in (18), with the series truncated at a finite order N and expanding, we arrive at a quadratic form, which is expressed as:

$$\mathcal{J}(\boldsymbol{x}) = \frac{1}{2}\boldsymbol{x}^T\boldsymbol{Q}\boldsymbol{x} - \boldsymbol{x}^T\boldsymbol{y}, \tag{19}$$

where $\boldsymbol{x}$ is a vector containing coefficients A_n, B_n up to the truncation order N, $\boldsymbol{Q}$ is a symmetric and positive definite matrix containing integrals of products between functions $\boldsymbol{w}_n^{(A)}, \boldsymbol{w}_n^{(B)}$ and $\boldsymbol{\tau}_n^{(A)}, \boldsymbol{\tau}_n^{(B)}$, and $\boldsymbol{y}$ is a vector containing integrals of products between functions $\boldsymbol{\tau}_n^{(A)}, \boldsymbol{\tau}_n^{(B)}$ and $\boldsymbol{v}$. The entries of matrix $\boldsymbol{Q}$ are computed analytically, and the components of vector $\boldsymbol{y}$ are computed by Gauss numerical integration for $\boldsymbol{v} = \psi_j\hat{\boldsymbol{\rho}}, \psi_j\hat{\boldsymbol{z}}$. The quadratic functional $\mathcal{J}$ in (19) reaches its minimum when $\boldsymbol{x}$ satisfies the linear system $\boldsymbol{Q}\boldsymbol{x} = \boldsymbol{y}$, which is solved by exploiting the block structure of $\boldsymbol{Q}$, in such a way that the coefficients A_n and B_n are in practice computed by simple forward and backward substitutions. This procedure allows us to evaluate the entries of matrix $\boldsymbol{K}^b$ given in (14), and thus to fully solve the boundary value problem (8).

2.6. Some remarks regarding the truncation radius choice

The influence of the truncation radius on the solution was studied in Ref. 17, by utilising a model problem which consists in a semi-spherical pit with exact analytical solution. This problem was numerically solved by the DtN-FEM for different radii R, and the obtained solution was then compared to the analytical solution. The physical constants were fixed at values within the typical ranges of a rock mass. Denoting by a the pit radius, the artificial boundary radius R was varied from $1.2a$ to $2a$ in increments of $0.1a$, while keeping the mesh size constant. The relative errors between analytical and numerical solution in the computational domain were computed in L^2-norm and H^1-seminorm as a function of R. The resulting errors were considerably small, even for a relatively close artificial boundary. For $R = 1.2a$, the relative errors in L^2-norm and H^1-seminorm were approximately 0.0079% and 0.78%, respectively, while for $R = 2a$, these errors were approximately 0.0046% and 0.56%, respectively. Therefore, the location of the artificial boundary affects to some extent the accuracy of the DtN-FEM procedure: A more distant location (i.e. a larger computational domain) results in a better accuracy, however, the accuracy achieved for a relatively close location (i.e. a small computational domain) is more than acceptable.

Regarding the problem we deal with in this paper, where the geometry corresponds to a open-pit slope, as there is no analytical solution available, the same analysis of relative errors cannot be performed. Nevertheless, it is reasonable to define a criterion to choose the radius R based upon the analysis carried out in Ref. 17, with the semi-spherical pit radius a assimilated to some characteristic length of the open pit slope, such as the maximum between the height H and the distance L defined later in Fig. 4. Therefore, any truncation radius between $1.2a$ and $2a$ provides a satisfactory accuracy, and the particular choice of R within this range is determined rather by the extent of the area around the pit that we desire to simulate.

3. Open-pit stability under the Mohr–Coulomb failure criterion

In order to characterise the stability of a particular open-pit geometry, we employ the Mohr–Coulomb failure criterion.[21] Given a stress tensor $\boldsymbol{\sigma}$ defined in every point of Ω, we denote the associated principal stresses as $\sigma_1 \geq \sigma_2 \geq \sigma_3$. The Mohr–Coulomb failure criterion is a set of linear equations relating shear stress τ as a function of normal stresses σ, therefore it might describe conditions where isotropic materials are prone to fail given that most of them have a limited range of shear stresses that can sustain. It only takes into account the smallest and the largest principal stresses σ_1 and σ_3, respectively, neglecting any intermediate principal stress σ_2 effects. The failure criterion is thus expressed by the relation:

$$|\tau| = S_0 + \tan\varphi\, \sigma, \tag{20}$$

where S_0 is the shear strength and φ is the friction angle, these two constants are material properties. Relationship (20) corresponds to a straight line in the plane (σ, τ) with slope $\tan\varphi$, as indicated in Fig. 3. A particular stress-state is represented by a Mohr semicircle, defined by σ_1 and σ_3. If a particular stress-state allows greater shear-stresses than the material shear-strength (the circle meets the straight line) then a failure is most probable. Various criteria have been presented as stability measures, slip-ratio[22,23] or stress-transfer[24–27] are popular

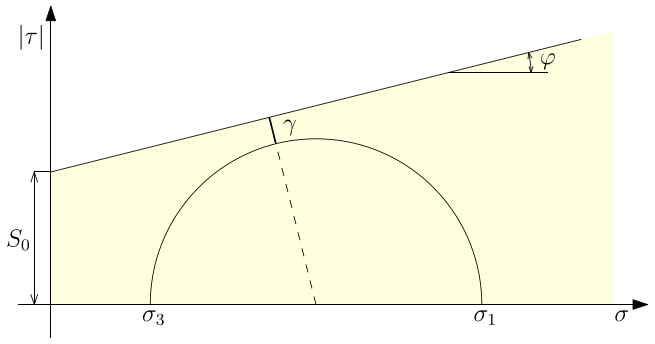

Fig. 3. Mohr–Coulomb failure criterion diagram.

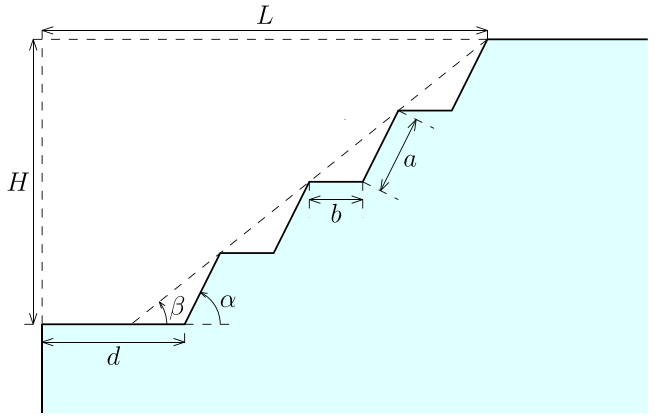

Fig. 4. Parameterised geometry of axisymmetric open-pit.

choices when particular fault directions are sought. We propose the distance γ as depicted in Fig. 3 as a simpler alternative for stability assessment given our choice of a homogeneous and isotropic material: the greater the distance the more stable the stress-state. From geometric considerations it is straightforward to calculate:

$$\gamma = \frac{1}{2}(\sigma_1 + \sigma_3)\sin\varphi + S_0\cos\varphi - \frac{1}{2}(\sigma_1 - \sigma_3). \tag{21}$$

If $\gamma > 0$, then the Mohr semicircle is completely under the straight line and the stress-state is stable. On the contrary, if $\gamma \leq 0$, then the semicircle meets the straight line and the stress-state is unstable.

4. Parameter space exploration

4.1. Parameterised open-pit geometry

In what follows, a regular parameterised geometry of open-pit is assumed, which is schematically described in Fig. 4. The main geometrical parameters are the overall slope height H, the number of benches n, the bench length a, the berm width b, the overall slope angle β and the bench face angle α (cf. Fig. 4). Notice that the bench height is given by H/n. Additionally, we consider the horizontal distances from the z-axis to the first bench d, and to the last bench L, as indicated in Fig. 4.

The following relationships between these parameters are valid:

$$L = d + na\cos\alpha + (n-1)b, \tag{22a}$$

$$H = (L - d + b)\tan\beta, \tag{22b}$$

$$H = na\sin\alpha, \tag{22c}$$

$$\frac{b}{a} = \frac{\sin(\alpha-\beta)}{\sin\beta}. \tag{22d}$$

Table 1
Open-pit numerical parameter examples.

Parameter	H	n	α	β	d	a	b	L
Units	m				m	m	m	m
Example 1	60	6	65°	50°	40	11.0330	3.7279	86.6181
Example 2	200	8	80°	70°	120	25.3857	4.6911	188.1030

Table 2
Physical parameters of numerical examples.

Parameter	ϱ	E	ν	S_0	φ
Units	kg m^{-3}	GPa		MPa	
Example 1	2700	10	0.2	20	35°
Example 2	2000	150	0.3	5	40°

In addition, it is clear that angles α and β must satisfy $\alpha > \beta$. In particular, if α becomes nearly equal to β, then the berm width b tends to zero, which may give rise to numerical singularities in the subsequent computations, due to the likely presence of degenerate triangles in the mesh. To avoid such complications, we restrict $\alpha \geq \beta + 10°$. In addition, as lengths L and d are linked by (22a) and (22b), only one of both needs to be previously fixed.

4.2. Numerical examples

To illustrate how the DtN-FEM works, we provide numerical examples. Two open-pit particular cases are solved and the solution is presented in each case. The two open-pit geometrical parameters are given in Table 1. The first example is a small open-pit with a relatively low slope angle and the second example is a medium size open-pit with a steeper slope angle. To choose suitable radii R for these two examples, we define as the "radius" of the open-pit slope the quantity $a = \max\{L, H\}$ and we employ the criterion established in Section 2.6. These radii are, for the first example $R = 150$ m ($R \approx 1.73a$) and for the second example $R = 400$ m ($R = 2a$). The respective meshes are depicted in Fig. 5. In both cases, a high degree of mesh refinement (between 1 m and 2 m) was imposed around benches and berms, to accurately describe the open-pit stability.

In the numerical simulations, pure geostatic stress was assumed as initial stress, with $g = 9.81$ m/s^2. The density ϱ, Young modulus E, Poisson ratio ν, shear strength S_0 and friction angle φ of both examples are presented in Table 2. Notice that the rock-mass of the second example is softer. This and the fact that the open-pit of the second example is larger and steeper, makes it more likely to be unstable.

Both numerical simulations took only a few seconds. Fig. 6 presents the displacement magnitudes. The domains have been deformed according to the computed displacement field multiplied by a factor, in order to visualise the deformation. It is observed that in both cases the open-pit bottom is displaced slightly upwards. This is due to the compressive nature of the initial geostatic stress. A larger displacement is seen in the second example, which is explained by the softer rock-mass in this case. Fig. 7 shows the von Mises stresses in both examples. Some stress accumulation arises at the bottom of every bench, in particular at the lowest one. This phenomenon is more evident in the second example. Fig. 8 shows the computed stability indicator γ in both examples. In the first case, γ remains positive and far from zero, then this open-pit slope configuration is stable. However, the lowest γ values occur at the benches bottom points, which suggest that those points are less stable. In the second example, γ has a clear minimum value at the lowest bench, which is negative. Therefore, this open-pit slope configuration is unstable and the lowest bench corresponds to a failure point. This fact is coherent with the stress accumulation observed at the same point in Fig. 7 (right).

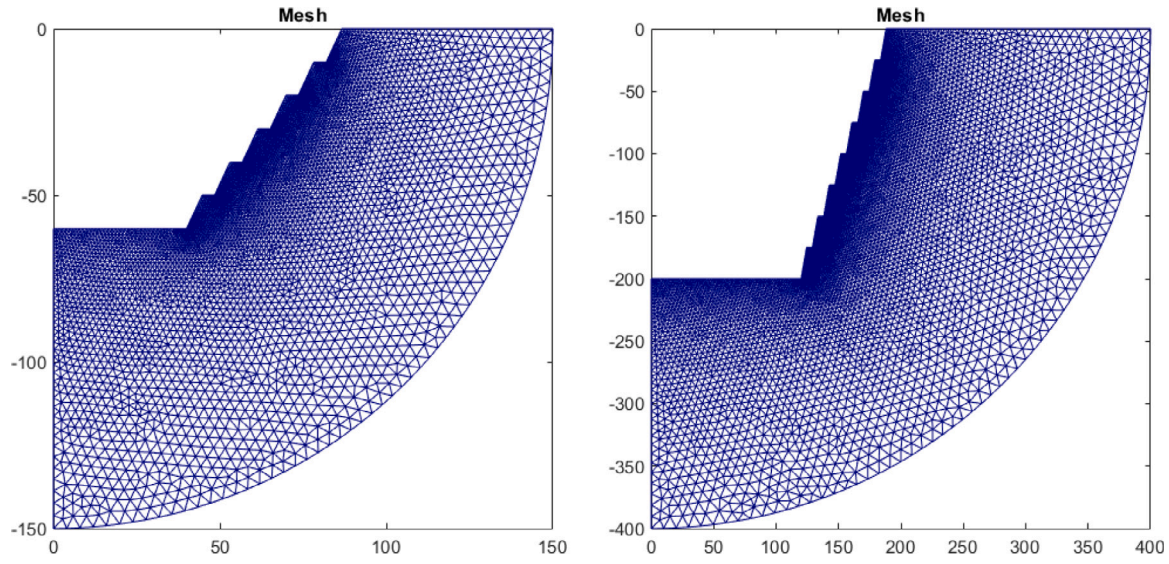

Fig. 5. FEM meshes of numerical examples 1 (left) and 2 (right).

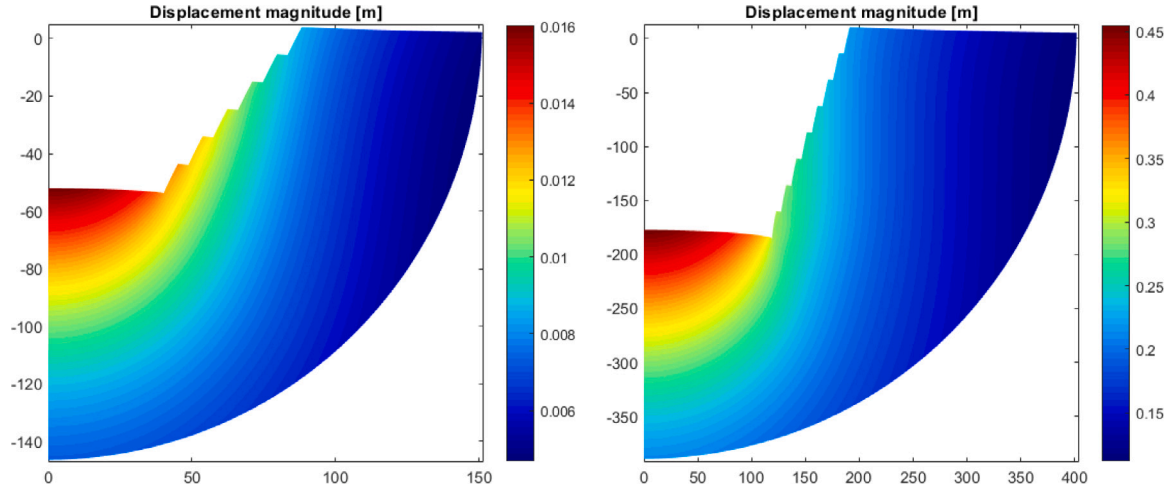

Fig. 6. Computed displacement magnitudes of numerical examples 1 (left) and 2 (right).

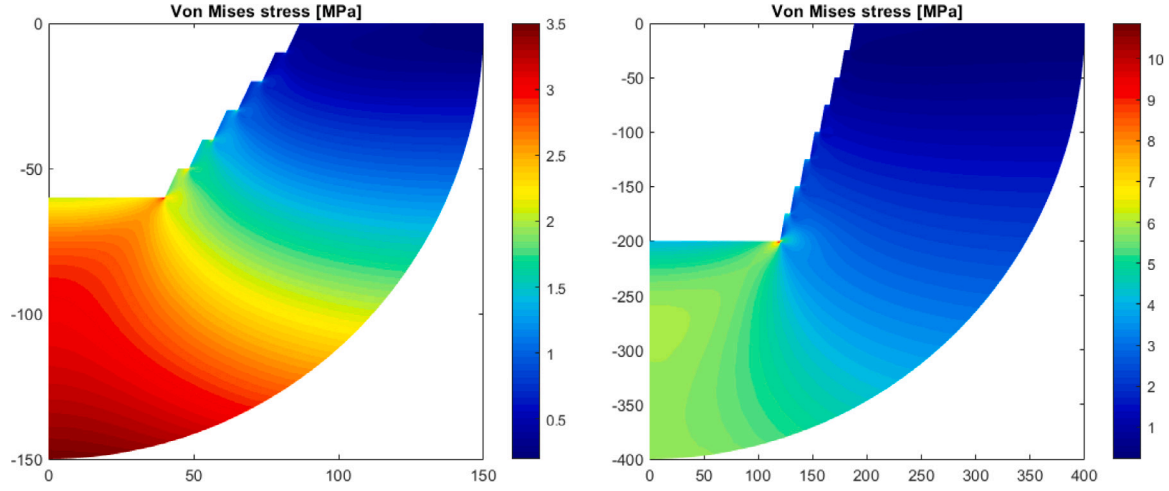

Fig. 7. Computed von Mises stresses of numerical examples 1 (left) and 2 (right).

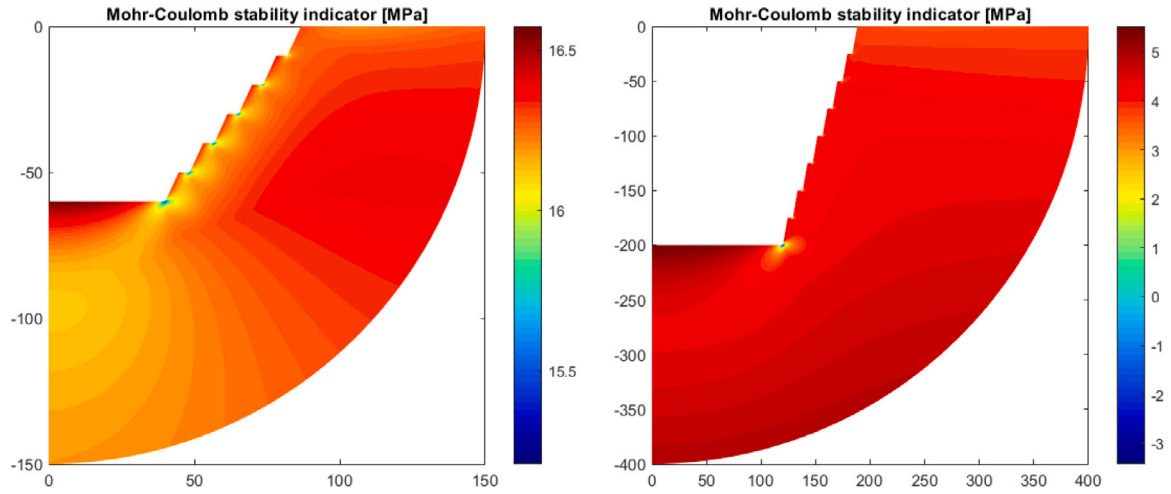

Fig. 8. Computed Mohr–Coulomb stability indicator of numerical examples 1 (left) and 2 (right).

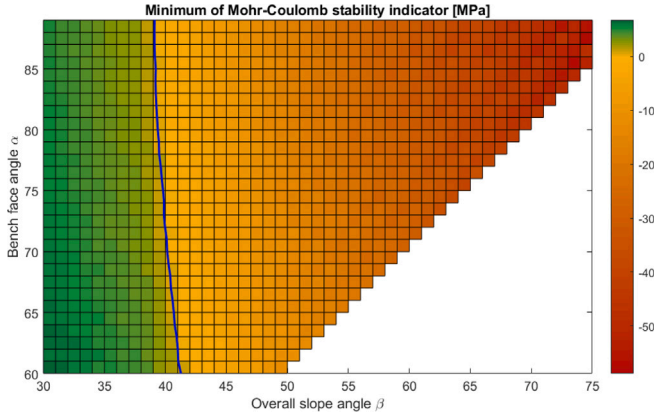

Fig. 9. Minimum stability indicator in function of α and β for $S_0 = 20$ MPa. (For interpretation of the references to colour in this figure legend, the reader is referred to the web version of this article.)

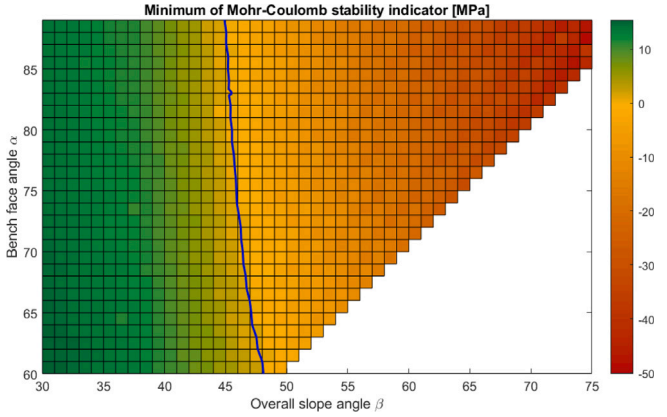

Fig. 10. Minimum stability indicator in function of α and β for $S_0 = 30$ MPa. (For interpretation of the references to colour in this figure legend, the reader is referred to the web version of this article.)

4.3. Solving multiple open-pit configurations

In what follows, multiple possible combinations of the angles α and β are considered. The open-pit slope resulting of each combination is numerically solved, in analogous way to the numerical examples of the previous subsection. This time, in all cases we assume a large open-pit, with an overall height $H = 1200$ m and $n = 12$ benches. Moreover, we suppose that the horizontal distance from the z-axis to the middle bench is fixed, which leads to a variable d, given by the relationship:

$$d = H - \frac{1}{2}\big(na\cos\alpha + (n-1)b\big). \tag{23}$$

The α and β ranges are assumed to be:

$$60^\circ \le \alpha < 90^\circ, \qquad 30^\circ \le \beta \le \min(75^\circ, \alpha - 10^\circ). \tag{24}$$

These ranges are discretised in equal steps $\Delta\alpha = \Delta\beta = 1^\circ$. The resulting (α, β) combinations number is 1055. Furthermore, to keep analysis simple a fixed truncation radius R is assumed, which needs to be large enough to contain all open-pit geometries. Among them, the largest open-pit slope radius (in the sense defined in Section 4.2) is approximately $a = 2181.5$ m. We then choose the radius value $R = 2620$ m ($R \approx 1.201a$), which fulfils the criterion established in Section 2.6. The E, ν, ϱ assumed values are presented in Table 3.

Three (α, β) parameter-space explorations are carried out for three values of the inherent shear strength, namely $S_0 = 20, 30, 40$ MPa.

Table 3
Open-pit physical parameters.

Parameter	ϱ	E	ν	φ
Units	kg m^{-3}	GPa		
Value	2800	80	0.25	30°

The remaining physical parameters are fixed to the values indicated in Table 3. For each value of S_0 and for every admissible combination of α and β, the stability indicator is calculated and its minimum is evaluated, which in all the cases occurs at the lowest bench bottom. When this minimum is positive, none of the points should fail and the open-pit slope configuration is stable. However, if the minimum is negative, then there are points that might fail and the open-pit slope configuration is unstable. Each parameter-space exploration took about one hour. Minimum-γ plots as functions of α and β are presented in Figs. 9–11, for $S_0 = 20, 30, 40$ MPa, respectively.

It is observed that the stability of a particular configuration depends mainly on the overall slope angle β. As might be expected a priori, stable configurations (green) are associated with low overall slope angles. Even for steep bench face angles, the configuration may be stable if β is low enough. On the other hand, higher overall slope angles lead to unstable configurations (red). The $\gamma = 0$ contour line location is shown in blue in the three cases. This line defines a stability boundary in the (α, β) plane, dividing it into a stable region on the left and an unstable region on the right. The stability-boundary location depends

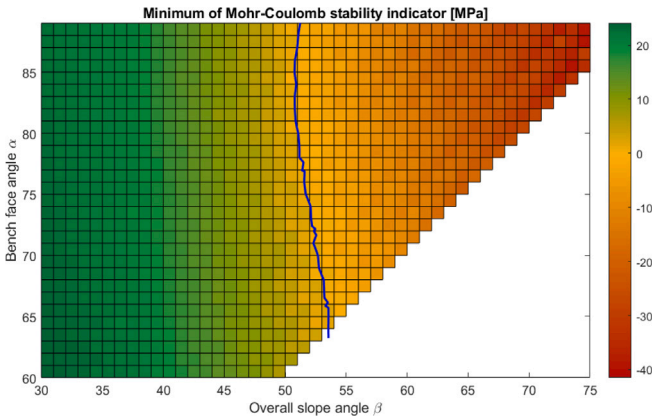

Fig. 11. Minimum stability indicator in function of α and β for $S_0 = 40$ MPa. (For interpretation of the references to colour in this figure legend, the reader is referred to the web version of this article.)

on S_0. For $S_0 = 20$ MPa, open-pit configurations are stable for $\beta < 39°$ and unstable for $\beta > 42°$. The stability depends on the bench face angle α for $39° \leq \beta \leq 42°$, which may be regarded as a transition zone. For $S_0 = 30$ MPa, the stability boundary moves to the right, increasing the stability region size. Open-pit slope configurations are stable for $\beta < 45°$ and unstable for $\beta > 48°$. The transition zone where the stability depends on α, this time corresponds to $45° \leq \beta \leq 48°$. Finally, when $S_0 = 40$ MPa, the stability region size increases even more. Open-pit slope configurations are stable for $\beta < 50°$ and unstable for $\beta > 54°$, yielding a transition zone $50° \leq \beta \leq 54°$, where the stability depends on α. The larger the inherent shear strength, the larger the amount of stable open-pit slope configurations.

5. Discussion and conclusions

A DtN-FEM approach for semi-infinite elastic domains has been applied to study open-pit stability in the axisymmetric case. The method is highly accurate, flexible and efficient, which allowed us to solve multiple open-pit slope configurations in a short amount of time. The open-pit stability was assessed by computing an indicator based upon the Mohr–Coulomb failure criterion, which is positive when the open-pit slope configuration is stable and negative otherwise. Other stability measures exist, and they might be explored as well, for instance the Hoek-Brown failure criteria in case of a fractured rock-mass. A regular open-pit geometry was considered, parameterised by the bench face angle α and the overall slope angle β, where α and β must satisfy some criteria to be considered geometrically admissible. Two numerical examples of open-pit geometries were simulated to illustrate how the method works. It was found that the benches bottom points are more likely to be unstable, in particular the lowest bench bottom point accordingly with the common knowledge. The space of parameters (α, β) was explored for three values of rock-mass shear strength S_0. The stability indicator was evaluated in every domain point and its minimum value was calculated. When this minimum is negative, there are points that might fail and the entire configuration is deemed unstable. Hence, regions of stability and instability were determined in the (α, β) space. It was found that the open-pit slope stability depends mainly on the overall slope angle. There are slope angle values β_1 and β_2, with $\beta_1 < \beta_2$, such that for $\beta < \beta_1$ the open-pit slope is stable, for $\beta > \beta_2$ is unstable, and for $\beta_1 \leq \beta \leq \beta_2$ the stability depends on the bench angle α. Furthermore, the stability region size depends on the shear strength S_0: the larger the S_0 value, the larger the β_1 and β_2 angles and the larger the stability region size as well, that is, more stable configurations exist in the (α, β)-plane. Given the flexibility of the method, very complicated geometries might be studied, with great precision, future work should focus on dropping the axisymmetry to include 3D geometries with variable properties, fractured geomaterials and time-dependence, specially the case of complex blasting sequences and induced seismicity forcing.

Declaration of competing interest

The authors declare that they have no known competing financial interests or personal relationships that could have appeared to influence the work reported in this paper.

Acknowledgements

The first author acknowledges the support of the Departamento de Ingeniería Matemática, Universidad de Concepción. The second author thanks INGMAT R&D Centre for allowing this research to be carried out.

Appendix. Explicit expressions for functions $\boldsymbol{w}_n^{(A)}, \boldsymbol{w}_n^{(B)}, \boldsymbol{\tau}_n^{(A)}, \boldsymbol{\tau}_n^{(B)}$

Let P_n be the Legendre polynomial of degree $n \in \mathbb{N}$ and $q(\cdot)$ the function defined as

$$q(\phi) = \frac{1}{1 - \cos\phi}.$$

Vector functions $\boldsymbol{w}_n^{(A)}, \boldsymbol{w}_n^{(B)}$ are defined by their components as

$$2\mu[w_n^{(A)}]_r(\phi) = -(2n+1)\big(\alpha_{2n} P_{2n}(\cos\phi) + \gamma_{2n} P_{2n+2}(\cos\phi)\big), \tag{A.1a}$$

$$2\mu[w_n^{(A)}]_\phi(\phi) = -\sin\phi\big(\alpha_{2n} P'_{2n}(\cos\phi) + \epsilon_{2n} P'_{2n+2}(\cos\phi)\big), \tag{A.1b}$$

$$2\mu[w_{-1}^{(B)}]_r(\phi) = -\big(1 - 2\nu + 4(1-\nu)\cos\phi\big), \tag{A.2a}$$

$$2\mu[w_{-1}^{(B)}]_\phi(\phi) = \sin\phi\big(3 - 4\nu - (1-2\nu)q(\phi)\big), \tag{A.2b}$$

$$2\mu[w_n^{(B)}]_r(\phi) = -(2n+2)\big(\alpha_{2n+2} P_{2n+1}(\cos\phi) + \gamma_{2n+1} P_{2n+3}(\cos\phi)\big), \tag{A.2c}$$

$$2\mu[w_n^{(B)}]_\phi(\phi) = -\sin\phi\big(\alpha_{2n+2} P'_{2n+1}(\cos\phi) + \epsilon_{2n+1} P'_{2n+3}(\cos\phi)\big), \tag{A.2d}$$

and tensor functions $\boldsymbol{\tau}_n^{(A)}, \boldsymbol{\tau}_n^{(B)}$ are defined by their components as

$$[\tau_n^{(A)}]_r(\phi) = (2n+1)(2n+2)\big(\alpha_{2n} P_{2n}(\cos\phi) + \beta_{2n} P_{2n+2}(\cos\phi)\big), \tag{A.3a}$$

$$\begin{aligned}[\tau_n^{(A)}]_\phi(\phi) \quad &= (\alpha_{2n} + \epsilon_{2n}) P'_{2n+1}(\cos\phi) - (2n+1)(2n+2) \\ &\times \big(\alpha_{2n} P_{2n}(\cos\phi) + (\alpha_{2n} - 2n + 2 - 4\nu) P_{2n+2}(\cos\phi)\big),\end{aligned} \tag{A.3b}$$

$$\begin{aligned}[\tau_n^{(A)}]_\theta(\phi) \quad &= -(4n+3)\big((2n+1)(2n+2)(1-2\nu) P_{2n+2}(\cos\phi) \\ &+ (2n - 1 + 2\nu) P'_{2n+1}(\cos\phi)\big),\end{aligned} \tag{A.3c}$$

$$[\tau_n^{(A)}]_{r\phi}(\phi) = \sin\phi\big((2n+2)\alpha_{2n} P'_{2n}(\cos\phi) + (2n+1)\alpha_{2n+1} P'_{2n+2}(\cos\phi)\big), \tag{A.3d}$$

$$[\tau_{-1}^{(B)}]_r(\phi) = 1 - 2\nu + 2(2-\nu)\cos\phi, \tag{A.4a}$$

$$[\tau_{-1}^{(B)}]_\phi(\phi) = -(1-2\nu)\big(1 + \cos\phi - q(\phi)\big), \tag{A.4b}$$

$$[\tau_{-1}^{(B)}]_\theta(\phi) = -(1-2\nu)\big(\cos\phi + q(\phi)\big), \tag{A.4c}$$

$$[\tau_{-1}^{(B)}]_{r\phi}(\phi) = -(1-2\nu)\sin\phi\big(1 - q(\phi)\big), \tag{A.4d}$$

$$[\tau_n^{(B)}]_r(\phi) = (2n+2)(2n+3)\big(\alpha_{2n+2} P_{2n+1}(\cos\phi) + \beta_{2n+1} P_{2n+3}(\cos\phi)\big), \tag{A.4e}$$

$$\begin{aligned}[\tau_n^{(B)}]_\phi(\phi) \quad &= \big(\alpha_{2n+2} + \epsilon_{2n+1}\big) P'_{2n+2}(\cos\phi) - (2n+2)(2n+3) \\ &\times \big(\alpha_{2n+2} P_{2n+1}(\cos\phi) + (\alpha_{2n+1} - 2n + 1 - 4\nu) P_{2n+3}(\cos\phi)\big),\end{aligned} \tag{A.4f}$$

$$\begin{aligned}[\tau_n^{(B)}]_\theta(\phi) \quad &= -(4n+5)\big((2n+2)(2n+3)(1-2\nu) P_{2n+3}(\cos\phi) \\ &+ (2n + 1 + 2\nu) P'_{2n+2}(\cos\phi)\big),\end{aligned} \tag{A.4g}$$

$$[\tau_n^{(B)}]_{r\phi}(\phi) = \sin\phi\,\alpha_{2n+2}\left((2n+3)P'_{2n+1}(\cos\phi) + (2n+2)P'_{2n+3}(\cos\phi)\right), \tag{A.4h}$$

where $n = 0, 1, 2, \ldots$ and

$$\alpha_{2n} = (2n+1)^2 - 2(1-\nu),$$
$$\beta_{2n} = (2n+2)(2n+5) - 2\nu,$$
$$\gamma_{2n} = (2n+2)(2n+5-4\nu),$$
$$\epsilon_{2n} = (2n+1)(2n-2+4\nu).$$

References

1. Givoli D. *Numerical Methods for Problems in Infinite Domains*. Amsterdam: Elsevier; 1992.
2. Telles J, Brebbia C. Boundary element solution for half-plane problems. *Int J Solids Struct*. 1981;17(12):1149–1158.
3. Dong C, Lo S, Cheung Y. Numerical solution for elastic half-plane inclusion problems by different integral equation approaches. *Eng Anal Bound Elem*. 2004;28:123–130.
4. Oliveira M, Dumnot N, Selvadurai A. Boundary element formulation of axisymmetric problems for an elastic halfspace. *Eng Anal Bound Elem*. 2012;36:1478–1492.
5. Zienkiewicz O, Emson C, Bettess P. A novel boundary infinite element. *Internat J Numer Methods Engrg*. 1983;19:393–404.
6. Zheng H, Wang F. The numerical manifold method for exterior problems. *Comput Methods Appl Mech Engrg*. 2020;364:112968.
7. Givoli D. Recent advances in the DtN FE method. *Arch. Comput. Method E.*. 1999;6(2):71–116.
8. Givoli D. Exact representations on artificial interfaces and applications in mechanics. *Appl. Mech. Rev.*. 1999;52(11):333–349.
9. Han H, Wu X. *Artificial Boundary Method*. Beijing-Berlin-Heidelberg: Tsinghua University Press and Springer-Verlag; 2013.
10. Han H, Wu X. Approximation of infinite boundary condition and its application to finite elements methods. *J Comput Math*. 1985;3:179–192.
11. Givoli D, Keller JB. A finite element method for large domains. *Comput Methods Appl Mech Engrg*. 1989;76(1):41–66.
12. Han H, Wu X. The approximation of the exact boundary conditions at an artificial boundary for linear elastic equations and its application. *Math Comp*. 1992;59(199):21–37.
13. Han H, Zheng C. Artificial boundary method for the three-dimensional exterior problem of elasticity. *J Comput Math*. 2005;23:603—618.
14. Givoli D, Vigdergauz S. Artificial boundary conditions for 2D problems in geophysics. *Comput Methods Appl Mech Engrg*. 1993;110(1–2):87–101.
15. Han H, Bao W, Wang T. Numerical simulation for the problem of infinite elastic foundation. *Comput Methods Appl Mech Engrg*. 1997;147:369–385.
16. Bao W, Han H. The direct method of lines for the problem of infinite elastic foundation. *Comput Methods Appl Mech Engrg*. 1999;175:157–173.
17. Godoy E, Boccardo V, Durán M. A Dirichlet-to-Neumann finite element method for axisymmetric elastostatics in a semi-infinite domain. *J Comput Phys*. 2017;328:1–26.
18. Boccardo V, Godoy E, Durán M. An efficient semi-analytical method to compute displacements and stresses in an elastic half-space with a hemispherical pit. *Adv. Appl. Math. Mech.*. 2015;7(3):295–322.
19. Sadd MH. *Elasticity: Theory, Applications, and Numerics*. Boston: Elsevier Butterworth-Heinemann; 2005.
20. Eubanks R. Stress concentration due to a hemispherical pit at a free surface. *J Appl Mech*. 1954;21:57–62.
21. Labuz J, Zang A. Mohr–Coulomb failure criterion. *Rock Mech Rock Eng*. 2012;45:975–979.
22. Lisle RJ, Srivastava DC. Test of the frictional reactivation theory for faults and validity of fault-slip analysis. *Geology*. 2004;32(7):569–572.
23. Morris A, Ferrill DA, Henderson DB. Slip-tendency analysis and fault reactivation. *Geology*. 1996;24(3):275–278.
24. Stein RS, King GC, Lin J. Change in failure stress on the southern san andreas fault system caused by the 1992 magnitude=7.4 Landers earthquake. *Science*. 1992;258(5086):1328–1332.
25. Stein RS, Lisowski M. The 1979 Homestead Valley earthquake sequence, California: Control of aftershocks and postseismic deformation. *J Geophys Res-Sol Ea*. 1983;88(B8):6477–6490.
26. Lin J, Stein RS. Stress triggering in thrust and subduction earthquakes and stress interaction between the southern San Andreas and nearby thrust and strike-slip faults. *J Geophys Res-Sol Ea*. 2004;109(B2).
27. King GC, Stein RS, Lin J. Static stress changes and the triggering of earthquakes. *B Seismol Soc Am*. 1994;84(3):935–953.